Nuclear Engineering and Technology 52 (2020) 2594–2600

Contents lists available at ScienceDirect

Nuclear Engineering and Technology

journal homepage: www.elsevier.com/locate/net

Original Article

Investigation of a blind-deconvolution framework after noise reduction using a gamma camera in nuclear medicine imaging

Kyuseok Kim [a], Min-Hee Lee [b, *], Youngjin Lee [c, **]

[a] Department of Radiation Convergence Engineering, Yonsei University, 1, Yonseidae-gil, Wonju-si, Gangwon-do, Republic of Korea
[b] Department of Pediatrics, Wayne State University School of Medicine, 3901, Beaubien St. Detroit, MI, USA
[c] Department of Radiological Science, Gachon University, 191, Hambakmoero, Yeonsu-gu, Incheon, Republic of Korea

ARTICLE INFO

Article history:
Received 12 December 2019
Received in revised form
20 April 2020
Accepted 28 April 2020
Available online 30 April 2020

Keywords:
Blind deconvolution
Noise reduction
Gamma camera
Nuclear medicine imaging
Quantitative evaluation of image performance

ABSTRACT

A gamma camera system using radionuclide has a functional imaging technique and is frequently used in the field of nuclear medicine. In the gamma camera, it is extremely important to improve the image quality to ensure accurate detection of diseases. In this study, we designed a blind-deconvolution framework after a noise-reduction algorithm based on a non-local mean, which has been shown to outperform conventional methodologies with regard to the gamma camera system. For this purpose, we performed a simulation using the Monte Carlo method and conducted an experiment. The image performance was evaluated by visual assessment and according to the intensity profile, and a quantitative evaluation using a normalized noise-power spectrum was performed on the acquired image and the blind-deconvolution image after noise reduction. The result indicates an improvement in image performance for gamma camera images when our proposed algorithm is used.

1. Introduction

X-ray photons and gamma rays using radioisotopes are routinely used in the field of diagnostic imaging worldwide. In particular, nuclear-medicine imaging encompasses all medical technologies that include radioactivity to diagnose disease. Among the imaging systems, the gamma camera (referred to as the Anger camera) with a scintillation detector, photomultiplier tubes, and a collimator is one of the most widely used devices in the field of nuclear medicine. It detects gamma rays emitted by radiopharmaceuticals [1,2]. In particular, the most common current examinations with the gamma camera for diagnosis are bone scans using a phosphate compound with a ^{99m}Tc label, brain perfusion scans, and myocardial perfusion scans [3–5]; these procedures depends on the patient's symptoms.

In gamma camera images, noise reduction is a major issue because the camera accumulates low gamma-ray photon counts, which are detected by a detector [6]. Numerous filters and denoising methods have been proposed to address the noise problem in gamma camera images. Notice that conventional filter-based [7–9] and iterative-based algorithms [10–12] have been uniquely impacted by denoising methods. Conventional median or average filters based on non-linear methods are generally used to reduce image noise and can achieve excellent timing resolution. Median and average filters focus on the zero mean with Gaussian noise and are calculated as follows [13]:

$$y_i = x_i + G_i \tag{1}$$

where y_i is the patch of the observed image, x_i is the original patch with the pixel center, and G_i is the Gaussian white noise. However, this method is a low-level image processing technique and has the major problem of low edge-preservation in images. To cope with this problem, iterative-based algorithms, such as total variation (TV) and non-local means (NLM), have been developed. In particular, the NLM noise-reduction algorithm is a more practical image-processing method, and its principle is based on the weighted average value of the pixel and similarity measurement [12]. Numerous studies on the excellent performance (image quality and processing time) of the NLM algorithm in medical photon-based images have been conducted. As demonstrated by *Lee* et al. in 2019, the contrast-to-noise ratio (CNR) and the coefficient of

* Corresponding author.
** Corresponding author.
E-mail addresses: min-hee.lee@wayne.edu (M.-H. Lee), yj20@gachon.ac.kr (Y. Lee).

https://doi.org/10.1016/j.net.2020.04.032

variation (COV) obtained by the NLM noise reduction algorithm are 1.34 and 1.71 times better, respectively, than that of the conventional median filter in high-energy X-ray images [14]. In addition, the timing resolution of the NLM noise-reduction algorithm is 6.70 times faster than that of the TV-based algorithm in a chest X-ray image with a 3D-printing nodule phantom, as studied by *Shim* et al., in 2019 [15].

However, all denoising methods including NLM inevitably result in image degradation with a blurring effect. To improve the blurring amplification, many conventional deblurring methods, including Bayesian, Wavelet transform, and TV approaches, have been used because of their low computation requirement and simplicity for processing [16]. In addition, the non-blind (unknown point spread function) technique has the problem of data loss. Although many methods have been proposed to improve deblurring problems in the image-processing field, the efficiency and accuracy of the algorithm fall short.

Thus, the purpose of this paper is to propose a highly efficient blind-deconvolution framework after a noise-reduction algorithm based on NLM with a gamma camera system. In this study, we performed a simulation using the Monte Carlo method and a real experiment with the gamma camera system. In addition, a visual assessment, intensity profile, and normalized noise-power spectrum (NNPS) were used to assess the effectiveness of our proposed algorithm.

2. Materials and methods

2.1. Proposed blind-deconvolution framework modelling

Fig. 1 shows an illustration of general image degradation with blurring due to the imaging system and the noise-reduction process. The degraded image, $g(x,y)$, is generated as follows:

$$g(x,y) = u(x,y) \otimes\otimes kernel_{system}(x,y) + n(x,y) \tag{2}$$

where $u(x,y)$ is the clean image; $kernel_{system}(x,y)$ is the degradation rate in the imaging system, including the finite focal-spot size and pixel size; $n(x,y)$ is the additional noise, including the Poisson noise and Gaussian noise; and $\otimes\otimes$ is the 2D convolution operator. Here, Eq. (2) follows a linear shift invariant [17].

We used the Anscombe transform (AT) [18,19] and NLM algorithm [20] for noise reduction. Generally, numerous noise-reduction algorithms suffer from mixed-noise images, which are composed of both Poisson and Gaussian noise. As a solution to this problem, AT is calculated as follows:

$$f_\sigma(g) = \begin{cases} \frac{2}{\alpha}\sqrt{\alpha g + \frac{3}{8}\alpha^2 + \sigma^2 - \alpha m}, & g > -\frac{3}{8}\alpha - \frac{\sigma^2}{\alpha} + m \\ 0, & g > -\frac{3}{8}\alpha - \frac{\sigma^2}{\alpha} + m \end{cases} \tag{3}$$

where α is a scaled parameter; and m and σ^2 are the mean and standard deviation of the Gaussian noise, respectively. We assume that the parameters are $\alpha = 1$, $\sigma = 0$, and $m = 0$ in the pure Poisson case in Eq. (4):

$$f(g) = \begin{cases} 2\sqrt{g + \frac{3}{8}}, & g > -\frac{3}{8} \\ 0, & g > -\frac{3}{8} \end{cases} \tag{4}$$

When $f_\sigma(g)$ is denoised, it is clear that $E\{f(g)|\widehat{f},\sigma\} = y$ because the Poisson noise is converted into an uncorrelated noise of the radiation photons. Assuming that $E\{f(g)|\widehat{f},\sigma\} = y$ is equal to $E\{g|\widehat{f},\sigma\} = y$, $\widehat{f}$ is obtained to use the direct algebraic inverse, $f^{-1}(y) = \frac{y^2}{4} - \frac{3}{8}$, of the inverse ATs. However, the result using the direct algebraic inverse is biased because $f_\sigma(g)$ is non-linear transform. To overcome this difficulty, we use the closed-form approximation of the exact, unbiased inverse transform [21]:

$$f^{-1}(g) = \frac{1}{4}y^2 + \frac{1}{4}\sqrt{\frac{3}{2}}y^{-1} - \frac{11}{8}y^{-2} + \frac{5}{8}\sqrt{\frac{3}{2}}y^{-3} - \frac{1}{8} \tag{5}$$

where y is the resultant Gaussian denoising using $f_\sigma(g)$. Here, we use the NLM algorithm to indicate noise reduction, and its algorithm is computed as follows:

$$y(s) = \frac{1}{Z(s)}\sum_{t\in N(s)} w(s,t)[f(g)](t) \tag{6}$$

$$w(s,t) = exp\left(-\frac{p(s,t)}{d^2}\right) \tag{7}$$

$$p(s,t) = \frac{1}{\delta}||g(\delta_s - \delta_t)||_2^2 \tag{8}$$

where $Z(s)$ is the normalized constant of the similarity between the two square patches between δ_s and δ_t at center pixels s and t, $N(s)$ is a large search window, and d is the proportional expected value of the distance both δ_s and δ_t.

After successful noise reduction, we obtain a more blurred image as follows:

$$y(x,y) = u(x,y) \otimes\otimes k_{total}(x,y) \tag{9}$$

where $k_{total}(x,y)$ is a total blur kernel, which is dependent on the x-ray imaging system and the noise algorithm. Eq. (9) depicts the ill-posed problem in which $u(x,y)$ and $kernel_{total}(x,y)$ are unknown. Fig. 2 shows a simplified flowchart for the blind-deconvolution in the blurred image, $y(x,y)$, to find $u(x,y)$. First, we find the initial sharp image prediction using Eqs. (10)–(12):

$$u^* = \underset{u}{argmin}||u \otimes\otimes k - y||_2^2 + \lambda||\nabla u||_0 \tag{10}$$

$$r^{(t+1)} = \underset{g}{argmin}\beta_u^{(t)}\nabla u^{(t)}|| - r||_2^2 + ||\lambda r||_0 \tag{11}$$

$$u^{(t+1)} = \underset{u}{argmin}||u \otimes\otimes k - y||_2^2 + \beta_u^{(t)}||\nabla u - r^{(t+1)}||_2^2 \tag{12}$$

where ∇u is substituted for r to calculate the half-quadratic splitting formulation [22] using the sub-problem of Eqs. (11) and (12)

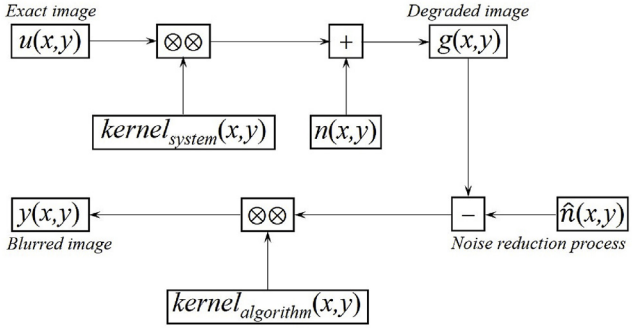

Fig. 1. Image degradation process with blurring and noise reduction process using kernel algorithm.

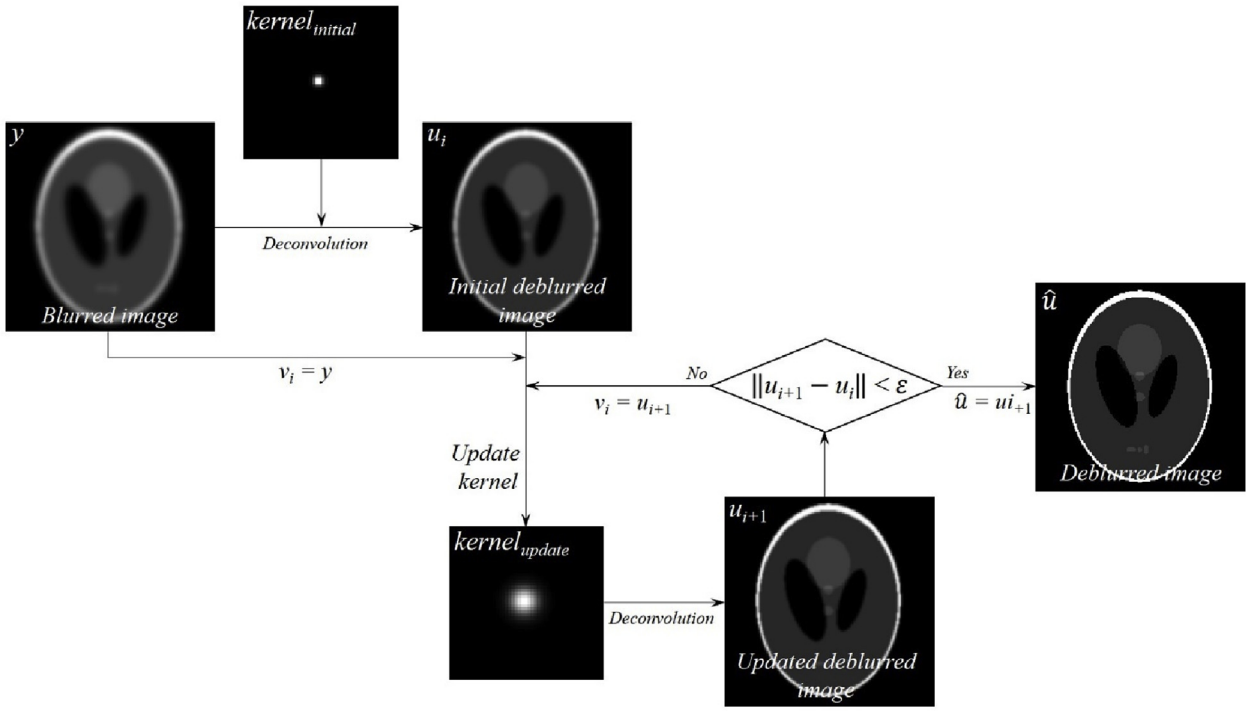

Fig. 2. Schematic description of our proposed blind-deconvolution in blurred image.

under the closed-form condition. β and λ are weight parameters to control the two terms; the regularization term used the l_0-norm gradient prior, which was introduced for natural image deconvolution by *Pan* et al. [23]. Then, we estimate the total blur kernel using the method of *Anger* et al. [24] as follows:

$$k^* = \underset{k \geqq 0, supp(k) \in \Omega}{argmin} ||u \otimes \otimes k - y||_2^2 + \rho||k_1|| + \gamma||\nabla k||_2^2 \tag{13}$$

$$h^{(t+1)} = \underset{u}{argmin}||u \otimes \otimes h - y||_2^2 + \beta_k^{(t)}||k^{(t)} - h||_2^2 + \gamma||\nabla h||_2^2 \tag{14}$$

$$k^{(t+1)} = \underset{k \geqq 0, supp(k) \in \Omega}{argmin} \beta_k^{(t)}||k - h^{(t+1)||_2^2} + \rho||k_1|| \tag{15}$$

where k is substituted for h to calculate the half-quadratic splitting formulation using the sub-problem of Eqs. (14) and (15) and ρ and γ also are balancing parameters; and Ω is a rectangular domain. Eq. (14) is effectively solved by two discrete Fourier transforms as follows:

$$h^{(t+1)} = \mathscr{F}^{-1}\left(\frac{\overline{\mathscr{F}(u)}\mathscr{F}(y) + \beta_k^{(t)}\mathscr{F}\left(k^{(t)}\right)}{|\mathscr{F}(u)|^2 + \beta_k^{(t)} + \gamma\left(|\mathscr{F}(\nabla_x)^2 + \mathscr{F}(\nabla_y)^2|\right)^2}\right) \tag{16}$$

where $\beta_k^{(0)} = 1$ and is multiplied by two at each iteration until the fifth iteration, and Eq. (15) can be solved using the soft shrinkage-thresholding method as follows:

$$k^{(t+1)}(x) = \begin{cases} \max\left(h^{(t+1)}(x) - \frac{\gamma}{\beta_k}, 0\right), & if\ x \in \Omega \\ 0 & otherwise. \end{cases} \tag{17}$$

Detail information of the splitting and proximal point methods for image deconvolution can be founded in references [25,26].

We acquire the updated deblurred image, μ_{i+1}, using the updated blur kernel k^*, and then check the mismatch between the updated deblurred image μ_{i+1}, and the pre-updated deblurred image μ_i, until the ε value of the difference error is reached. Finally, the deblurred image, $\hat{u}$, is obtained by using the blind deconvolution process.

2.2. Simulation and experimental conditions

The Monte Carlo simulation tool using Geant4 Applications for Tomographic Emission (GATE) version 6 was used in this study to simulate the gamma camera system. We designed the ^{99m}Tc source using 100,000-Bq activity with a hot-rod phantom. The phantom image was acquired with a 900-s scan time and a cadmium-telluride detector with a 44.8 × 44.8 mm^2 area, using a parallel-hole collimator. In this study, a statistical noise distribution was modeled on the GATE simulation to obtain the applied image.

A gamma camera system (Discovery NM/CT 670, GE Healthcare) consisting of a parallel-hole collimator was used in the experimental study. In addition, we used a Jaszcazk phantom with a ^{99m}Tc source, and the source-to-collimator distance was 21 cm.

2.3. Evaluation of image quality

The evaluation parameters of visual assessment, intensity profile, and NNPS were used to evaluate the effectiveness of our proposed blind-deconvolution framework after using the noise-reduction algorithm based on NLM. The NNPS is calculated as follows [27]:

$$\mathrm{NNPS}(u,v) = \frac{\mathrm{NPS}(u,v)}{(\text{mean signal})^2} \tag{18}$$

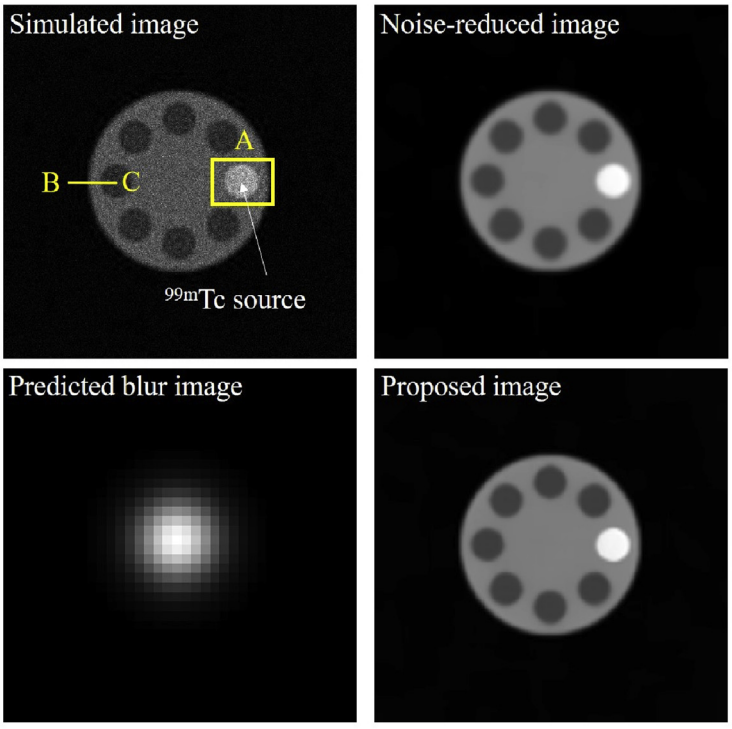

Fig. 3. (a) Result images, and (b) enlarged images using the box-A region with Monte Carlo simulation.

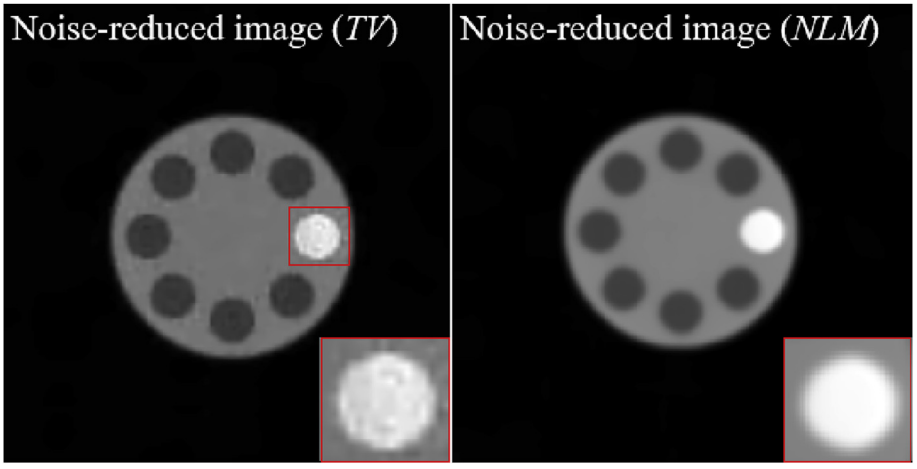

Fig. 4. Comparison result of the noise reduction image with TV algorithm (left) and that of NLM algorithm (right).

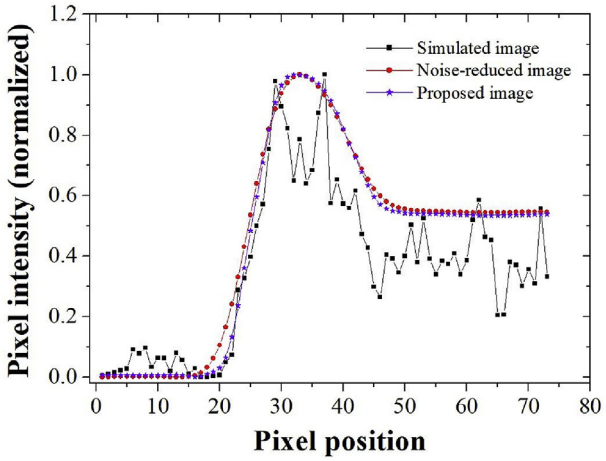

Fig. 5. Calculated profiles of the Monte Carlo simulation image using the BC-line region in Fig. 3 (a).

$$\mathrm{NPS}(u_n, v_k) = \lim_{N_x N_y, M\to\infty} \frac{\Delta x \Delta y}{M \cdot N_x N_y} \sum_{m=1}^{M} < \left| \sum_{j=1}^{N_x} \times \sum_{l=1}^{N_y} (I(x_j, y_l) - S(x,y)) \exp\left(-2\pi i \left(u_n x_j + v_k y_j \right) \right) \right|^2 > \tag{19}$$

where u and v are the spatial frequency conjugates, Δx and Δy are the pixel spacing, N_x and N_y are number of pixels in the X and Y directions (e.g., Δx and Δy are both 3 mm and N_x and N_y are both 64 pixels, empirically), M is the number of ensemble averages, $I(x_j, y_l)$ is the image intensity at the (x_j, y_l) pixel location, and $S(x, y)$ is the mean intensity. 2D NNPS is converted 1D data form using the radial averaging method. Note that the smaller NNPS vales per spatial frequency, the better noise characteristic in the measured data.

3. Results and discussion

In gamma camera imaging, a non-linear filter including a median filter is a major denoising method that uses an image-processing technique. Although a non-linear filter with common window-kernel size is easy to use, it has the drawbacks of relatively low denoising efficiency and low preservation of edge information. To address these problems, iterative-based algorithms including NLM and a non-blind technique have been developed. However, these two methods still have problems with blurring effects and data loss in gamma camera imaging. Thus, we propose a highly efficient blind-deconvolution framework based on both simulation and real experiments of the NLM denoising process in a gamma camera system.

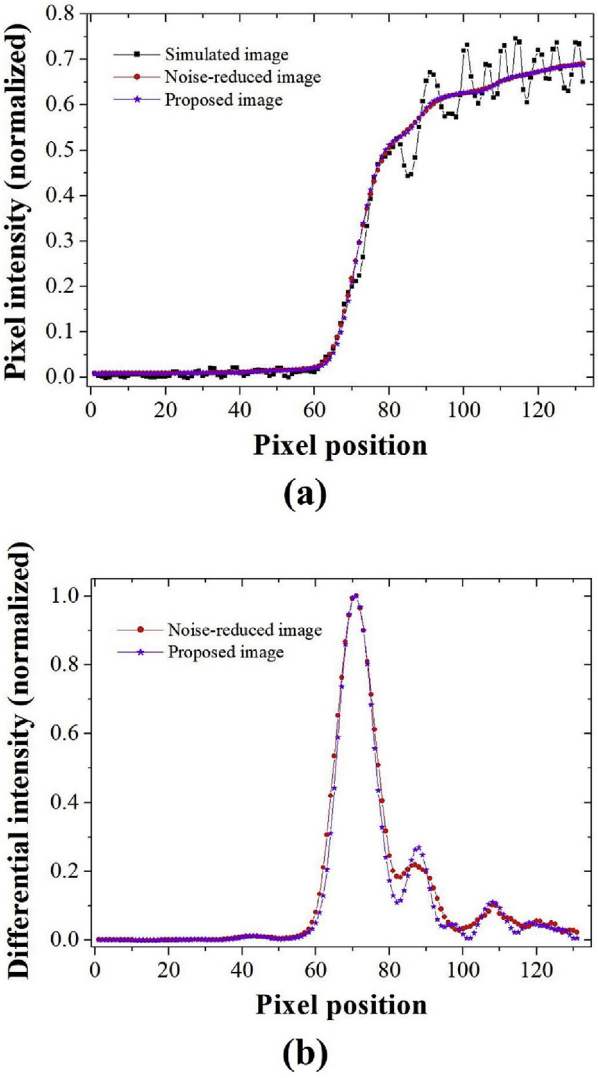

Fig. 7. (a) Measured profiles of the experimental image using the AB-line region in Fig. 6 (a), and (b) differential profiles of the noise-reduced and proposed images.

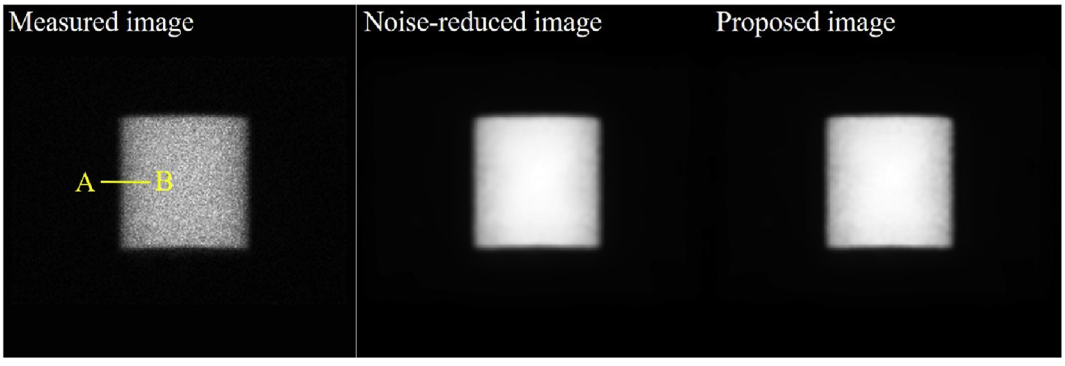

Fig. 6. Experimental result images using the real gamma camera system.

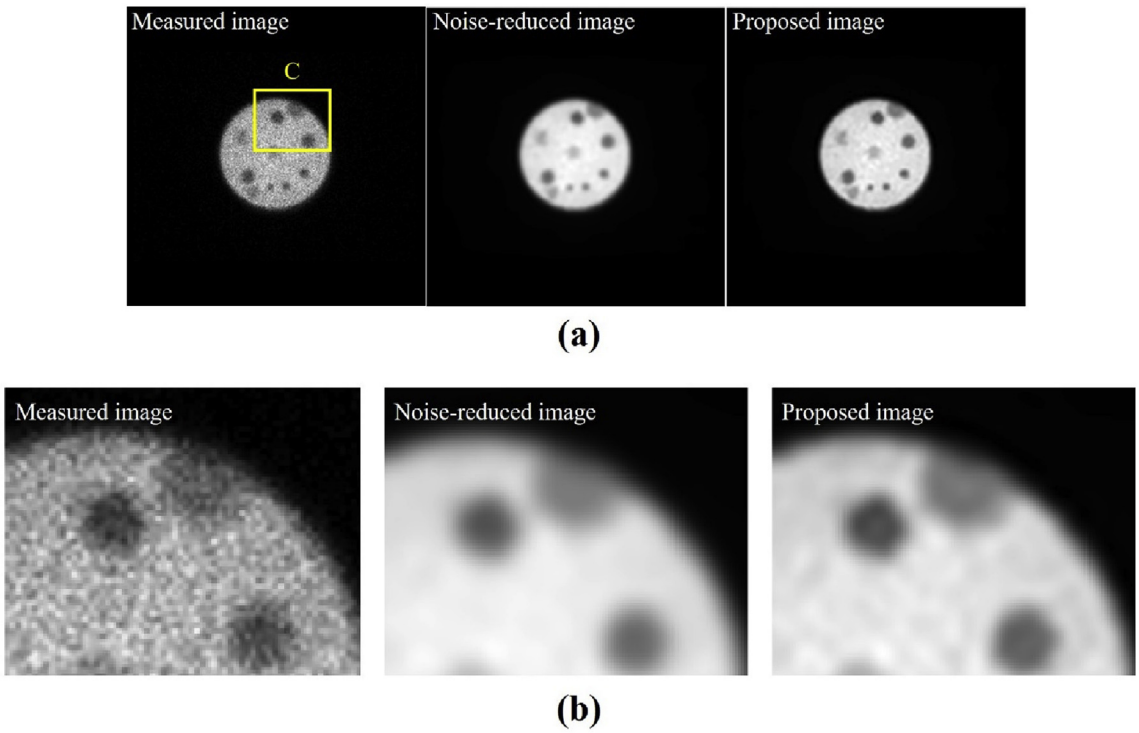

Fig. 8. (a) Result images and (b) enlarged images using the box-C region with the real gamma camera system.

Fig. 3 shows the Monte Carlo simulation results of a (a) simulated image (left top), noise-reduced image (top right), predicted blur image (bottom left), and proposed image (bottom right); and the (b) enlarged images of the simulated image (left), noise-reduced image (middle), and proposed image (right) in box A. Fig. 4 shows the comparison result of the noise reduction image using the TV algorithm (left) and the NLM algorithm (right). Its result indicated that the NLM algorithm effectively performed the noise reduction without additional artifact (i.e., cartoon artifact) because it can be seen that the method of the smoothing by assigning the weights to similar information in the surrounding the local-area is a suitable method of the minimizing the artifacts. From a qualitative analysis, we confirm that the proposed algorithm accurately recovered the blur artifact from only the noise-reduced image. To objectively compare the performance of the proposed framework, Fig. 5 shows the measured profiles of the simulated, noise-reduced, and proposed images in Fig. 3(a), line BC. The profile of the proposed image is sharper than that of the noise-reduced image indicated by the red arrows.

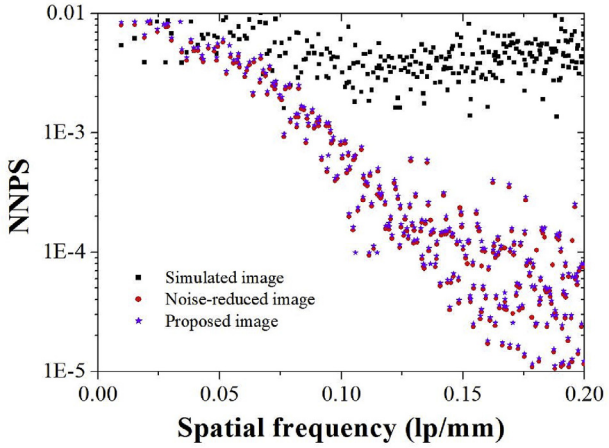

Fig. 9. 1D NNPS plot result with respect spatial frequency.

Fig. 6 shows the experiment results using the Jaszcazk phantom (side view) of the measured image (left), noise-reduced image (middle), and proposed image (right). Fig. 7 shows the profiles of (a) the measured, noise-reduced, and proposed images in Fig. 6, line AB; and (b) the differential profiles of the noise-reduced and proposed images. Here, the full-width at half maximum of differential profiles of the proposed image is approximately 11 pixels, which is approximately 0.7 times smaller than that of the noise-reduced image.

Fig. 8 shows the experiment images using the Jaszcazk phantom (top view) of the (a) measured image (left), noise-reduced image (middle), and proposed image (right); and (b) enlarged images of box A. These results reflect that the proposed framework accurately restored the blurring both experimentally and in the simulation study. Fig. 9 shows the 1D NNPS plot of the measured, noise-reduced, and proposed images. The 1D NNPS of the noise-reduced and proposed images are located below that of the measured image, and only slight differences were observed between the noise-reduced and proposed images. Therefore, the proposed framework implemented the blind-deconvolution without additional noise amplification.

4. Conclusion

We showed improved results with highly efficient blind-deconvolution framework after the noise-reduction algorithm based on NLM in the gamma camera image. In conclusion, our results demonstrated that the proposed method can enhance images with far more computationally demanding algorithms in the gamma camera system.

Declaration of competing interest

The authors declare that they have no known competing financial interests or personal relationships that could have appeared to influence the work reported in this paper.

Acknowledgments

This research was supported by the National Research Foundation of Korea (NRF-2019R1F1A1062811). In addition, Min-Hee Lee and Youngjin Lee contributed equally to this study.

References

[1] H.O. Anger, Scintillation camera with multichannel collimators, J. Nucl. Med. 5 (1964) 515–531.
[2] T.E. Peterson, L.R. Furenlid, SPECT detectors: the Anger camera and beyond, Phys. Med. Biol. 56 (2011) R145–R182.
[3] R.J. Shearer, A.R. Constable, M. Girling, W.F. Hendry, J.D. Fergusson, Radioisotopic bone scintigraphy with the gamma camera in the investigation of prostatic cancer, Br. Med. J. 2 (1974) 362–365.
[4] K. Kimura, K. Hashikawa, H. Etani, A. Uehara, T. Kozuka, H. Moriwaki, Y. Isaka, M. Matsumoto, T. Kamada, H. Moriyama, H. Tabuchi, A new apparatus for brain imaging: four-head rotating gamma camera single-photon emission computed tomograph, J. Nucl. Med. 31 (1990) 603–609.
[5] G.U. Hung, Y.F. Wang, H.Y. Su, T.C. Hsieh, C.L. Ko, R.F. Yen, New trends in radionuclide myocardial perfusion imaging, Acta Cardiol. Sin. 32 (2016) 156–166.
[6] J.D. Sain, H.H. Barrett, Performance evaluation of a modular gamma camera using a detectability index, J. Nucl. Med. 44 (2003) 58–66.
[7] C.V. Cannistraci, A. Abbas, X. Gao, Median modified Wiener filter for nonlinear adaptive spatial denoising of protein NMR multidimensional spectra, Sci. Rep. 5 (2017), https://doi.org/10.1038/srep08017.
[8] N.H. Mahmood, M.R.M. Razif, M.T.A.N. Gany, Comparison between median, unsharp and Wiener filter and its effect on ultrasound stomach tissue image segmentation for pyloric stenosis, Int. J. Appl. Sci. Technol. 1 (2011) 218–226.
[9] P. Patidar, M. Gupta, S. Srivastava, A.K. Nagawat, Image de-noising by various filters for different noise, Int. J. Comput. Appl. 9 (2010) 45–50.
[10] K. Seo, S.H. Kim, S.H. Kang, J. Park, C.L. Lee, Y. Lee, The effect of total variation (TV) technique for noise reduction in radio-magnetic X-ray image: quantitative study, J. Magnetics 21 (2016) 593–598.
[11] C.R. Park, Y. Lee, Fast non-local means noise reduction algorithm with acceleration function for improvement of image quality in gamma camera system: a phantom study, Nucl. Eng. Technol. 51 (2019) 719–722.
[12] H.V. Bhujle, B.H. Vadavadagi, NLM based magnetic resonance image denoising – a review, Biomed. Signal Process Contr. 47 (2019) 252–261.
[13] X. Wang, H. Wang, J. Yang, Y. Zhang, A new method for nonlocal means image denoising using multiple images, PloS One 11 (2016), https://doi.org/10.1371/journal.pone.0158664.
[14] S. Lee, H. Cho, Y. Lee, High-energy industrial 2D X-ray imaging system with effective nonlocal means denoising for nondestructive testing, Nucl. Instrum. Methods Phys. Res. A 925 (2019) 212–216.
[15] J. Shim, M. Yoon, Y. Lee, Quantitative study of fast non-local means-based denoising filter in chest X-ray imaging with lung nodule using three-dimensional printing, Optik 179 (2019) 1180–1188.
[16] Z.A. Ameen, G. Sulong, A novel Zohair filter for deblurring computed tomography medical images, Int. J. Imag. Syst. Technol. 25 (2015) 265–275.
[17] R. Gonzalez, R. Woods, Digital Image Processing, third ed., Pearson Education, New Jersey, 2009.
[18] J.L. Starck, F. Murtagh, A. Bijaoui, Image Processing and Data Analysis, Cambridge University Press, Cambridge, 1998.
[19] M. Makitalo, A. Foi, Optimal inversion of the Anscombe transformation in low-count Poisson image denoising, IEEE Trans. Image Process. 20 (2010) 99–109.
[20] A. Buades, B. Coll, J. Morel, A review of image denoising algorithms, with a new one, Multiscale Model. Simul. 4 (2006) 490–530.
[21] M. Makital, A. Foi, A closed-form approximation of the exact unbiased inverse of the anscombe variance-stabilizing transformation, IEEE Trans. Image Process. 20 (2011) 2697–2698.
[22] D. Geman, C. Yang, Nonlinear image recovery with half-quadratic regularization, IEEE Trans. Image Process. 4 (1995) 932–946.
[23] J. Pan, Z. Su, Fast l0-regularized kernel estimation for rubust motion deblurring, IEEE Trans. Signal Processing Letters 20 (2013) 841–844.
[24] J. Anger, M. Delbracio, G. Facciolo, Effective Blind Deblurring under High Noise Levels, 2019 arXiv:1904.09154.
[25] D. Sudipto, O. Michailovich, Blind deconvolution of medical ultrasound images using variable splitting and proximal point methods, in: 2011 IEEE International Symposium on Biomedical Imaging: from Nano to Macro, 2011, https://doi.org/10.1109/ISBI.2011.5872341. Chicago, IL, USA, 09 June.
[26] S. Chen, X. Wang, O. Elgendy, Plug-and-play ADMM for image restoration: fixed-point convergence and applications, IEEE Trans Comput Imag 3 (2016) 84–98.
[27] J. Dobbins III, E. Samei, N. Ranger, Y. Chen, Intercomparison of methods for image quality characterization. II. Noise power spectrum, Med. Phys. 33 (2006) 1466–1475.